

Multifunctional adaptive optics optical coherence tomography allows cellular scale reflectometry, polarimetry, and angiography in the living human eye

KAZUHIRO KUROKAWA* AND MORGAN NEMETH

Discoveries in Sight Research Laboratories, Devers Eye Institute, Legacy Research Institute, Legacy Health, Portland, OR 97232 USA

**kkurokawa@deverseye.org*

Abstract: Clinicians are unable to detect glaucoma until substantial loss or dysfunction of retinal ganglion cells occurs. To this end, novel measures are needed. We have developed an optical imaging solution based on adaptive optics optical coherence tomography (AO-OCT) to discern key clinical features of glaucoma and other neurodegenerative diseases at the cellular scale in the living eye. Here, we test the feasibility of measuring AO-OCT-based reflectance, retardance, optic axis orientation, and angiogram at specifically targeted locations in the living human retina and optic nerve head. Multifunctional imaging, combined with focus stacking and global image registration algorithms, allows us to visualize cellular details of retinal nerve fiber bundles, ganglion cell layer somas, glial septa, superior vascular complex capillaries, and connective tissues. These are key histologic features of neurodegenerative diseases, including glaucoma, that are now measurable in vivo with excellent repeatability and reproducibility. Incorporating this noninvasive cellular-scale imaging with objective measurements will significantly enhance existing clinical assessments, which is pivotal in facilitating the early detection of eye disease and understanding the mechanisms of neurodegeneration.

1. Introduction

Neurodegenerative diseases, including glaucoma, often have profound impacts on the well-being of affected individuals, their families, and communities. The prevalence of these diseases will increase because of population aging and growth [1]. Strategic actions are needed to prevent, treat, and manage care at all levels [2–4]. One area that has shown significant progress is biomarker research and development (e.g., blood testing [5]). Still, current standard clinical diagnostic measurements lack the ability to detect early signs of these diseases and their progressions. For example, common clinical measures for glaucoma, such as visual field loss and retinal nerve fiber layer/ganglion cell layer (RNFL/GCL) thinning, are unable to detect loss or damage at the level of a single cell. Substantial retinal ganglion cell (RGC) losses or their dysfunctions could have already occurred when clinically diagnosed. Thus, clinical management is mainly based on findings that represent moderate, irreversible damage. Besides early detection, therapeutic interventions in neuroprotection and restoration require novel outcome measures to determine efficacy. To this end, we need novel biomarkers that may represent reversible aspects of disease pathophysiology and neurodegeneration.

High-resolution retinal imaging offers a unique opportunity to tackle some of the major obstacles in diagnosing and predicting the progression of glaucoma and other neurodegenerative diseases and to understand disease pathophysiology [6–11]. Particularly, adaptive optics optical coherence tomography (AO-OCT) imaging technology is a rapidly evolving, state-of-the-art, noninvasive, and label-free imaging modality [12,13] that enables direct assessment of the health of individual cells, including RGCs, their axons, the glial cells integral to the maintenance of retinal health, as well as microvasculature, in a repeatable manner over time, all in the living human eye [12,14,15]. Notably, investigators have been able to

directly measure the rate of GCL soma loss in thousands of GCL somas over years in the living human eye [16–18]. This direct approach has the potential to differentiate normal aging from glaucomatous progression in less time than clinical instruments.

AO-OCT also offers the capability of visualizing histologic details of pathophysiology and cellular damage in vivo, such as (1) the detailed cross-sectional view of individual retinal nerve fiber bundles (RNFBs) [19–22] and individual axons in the macula [18,22]; (2) the detailed characterization of lamina cribrosa (LC) microarchitecture in 3D (such as pores and beams) where it is thought that RGC axons are being primarily injured [23,24]; (3) the quantification of tissue intrinsic optical properties, such as form birefringence (a property of ultrastructure) of RGC axons (or nerve fibers) [25] and of collagenous tissue such as LC beams, by employing the principle of polarimetry; (4) the detection of the blood flow and where it is deficient based on the motion contrast technique [26–30]; (5) the detailed characterization of macrophage-like cells [18,31]. More recently, phase-sensitive AO-OCT permits the detailed analysis of nanometer-scale change in optical path length differences (ΔOPL) in response to a visible stimulus [32–35]. As such, there is great potential for AO-OCT to improve both the study of disease pathophysiology and its translation to clinical care.

However, ophthalmoscopic manifestations of glaucoma and other neurodegenerative diseases are heterogeneous and interdependent within the retina and optic nerve head (ONH), often complicating their implications and, thus, treatment and care. We need safe, accurate, and efficient biomarkers to capture and unravel critical aspects of the disease and its progression, including neuronal loss, axonopathy, dendritic atrophy, retinal gliosis, and vascular dysfunction over time [4,8]. To address these complexities, we have developed a new high-resolution multifunctional AO-OCT imaging instrument, specifically committed to in-depth investigations into various aspects of neurodegeneration in the living human eye at the cellular scale, such as normal aging, glaucoma, and other neurodegenerative diseases, including diabetes, Alzheimer's Disease, Parkinson's Disease, and multiple sclerosis. We have realized such a versatile solution by integrating well-established optical imaging techniques, including quantitative three-dimensional morphometry [22,23,36,37], elastography [38–41], polarimetry [25,42–45], reflectometry [18], angiography [18,26–30], and optoretinography [32–35]. More specifically, we have incorporated a polarization channel and a fluorescent/visual stimulation channel into a conventional AO-OCT system by combining novel optical system design, systematic implementation, and extensive processing software, such as volume reconstruction, registration, and composition algorithms.

Here, we describe our process of designing, building, and testing a newly developed multifunctional AO-OCT imaging system. We have designed this imaging system under strict constraints to achieve high-performance imaging by minimizing optical loss, wavelength dependency, specular reflection, and optical aberration such as astigmatism and coma as well as coating-induced polarization aberration. In addition, we have integrated a polarization-sensitive OCT (PS-OCT) interferometer with bulk and fiber optics, enabling highly repeatable and reproducible polarization measurements without introducing ghost images, sacrificing depth range, or reducing imaging speed like other PS-OCT systems. During testing, we have demonstrated our multifunctional AO-OCT-based methods toward quantitative reflectometry, polarimetry, and angiography (Fig. 1), a subset of its functions, as a proof of concept. The imaging performance is assessed in a model eye and then three healthy subjects in which we systematically and longitudinally survey selected fundus locations, including ONH, peripapillary, and arcuate (Bjerrum) regions. We choose these specific locations for the following reasons: (1) Peripapillary retinal nerve fiber layer (pRNFL) thickness has been a prominent structural measure of glaucoma [6,7,9–11] and other neurodegenerative diseases [8]. Similarly, recent attention focuses on the peripapillary vasculature (peripapillary radial capillaries; PRCs) [46] as well as pRNFL reflectance [47–49] and retardance (or birefringence) [50–52]. To further characterize their structural and intrinsic optical properties, we need a detailed view of pRNFL in 3D. (2) ONH is another prominent site of neuronal

damage in normal aging, glaucoma [53–60], and other neurodegenerative diseases [8]. Discerning ONH tissue microstructures, their deformation and remodeling, including reactive gliosis and fibrosis, is central to further understanding of underlying pathophysiology [53,61]. (3) Examining the region along an arcuate RNFL bundle could reveal the time course, sequence of pathophysiological events, and their correlations to established clinical manifestations, such as RNFL/minimum rim width (MRW) thinning, RGC functional loss, and alterations of retinal blood flow before substantial loss of RGCs [62–66]. For each location, we have iterated on and developed a repeatable AO-OCT imaging method to allow for larger-scale studies. We also have improved the multifunctional AO-OCT measurements by combining focus stacking and global image registration methods [67]. In doing so, we have shown our first multifunctional AO-OCT imaging results that expose the details of RNFBs, GCL somas, glial cells, superior vascular complex capillaries, and connective tissues in the living human retina and ONH, key clinical features of neurodegeneration. Going forward, we discuss key advancements, feasibility and translational aspects of the multifunctional AO-OCT-based approach, but at this time we make no attempts to test a specific hypothesis or to make a formal comparison in this paper.

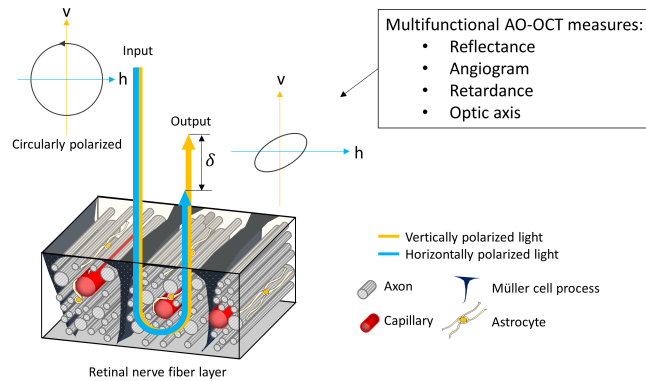


Fig. 1. Cellular-scale multifunctional imaging of the retinal nerve fiber layer using AO-OCT. Measuring AO-OCT-based reflectance, angiogram, retardance, and optic axis orientation reveals cellular and subcellular features (e.g., individual retinal nerve fiber bundles and striated glial septa), polarization properties (e.g., well-being of nerve fiber parallel structure, density, and orientation), and their dynamics (e.g., capillary blood flow), all of which are key clinical features in glaucoma and other neurodegenerative diseases.

2. Methods

We describe methods in two sections: Section 2.1 describes the Legacy Devers AO-OCT imaging system hardware used in this study. Section 2.2 describes the real-time control and offline processing software to compute AO-OCT-based reflectance, retardance, and angiogram. Section 2.3 describes the imaging parameters used for testing the imaging performance of the newly developed multifunctional AO-OCT.

2.1 AO-OCT imaging system

We developed a new multifunctional high-resolution retinal imaging system at Discoveries in Sight Research Laboratories / Devers Eye Institute, based on AO-OCT that combines a point-scanning spectral-domain OCT (SD-OCT) with a hardware-based AO [68,69,12,70]. We realized the multifunctionality by incorporating polarization and fluorescence/stimulation channels, as shown in Fig. 2. Further details are described in [Supplemental Section S1](#), whereas [Table 1](#) summarizes the key parameters of the imaging device. Optical power delivered to the eye was below 420 μ W for the AO-OCT imaging beam, which was well below the maximum permissible beam power allowed by the American National Standards Institute guidelines for the safe use of laser for human retinal imaging [71,72].

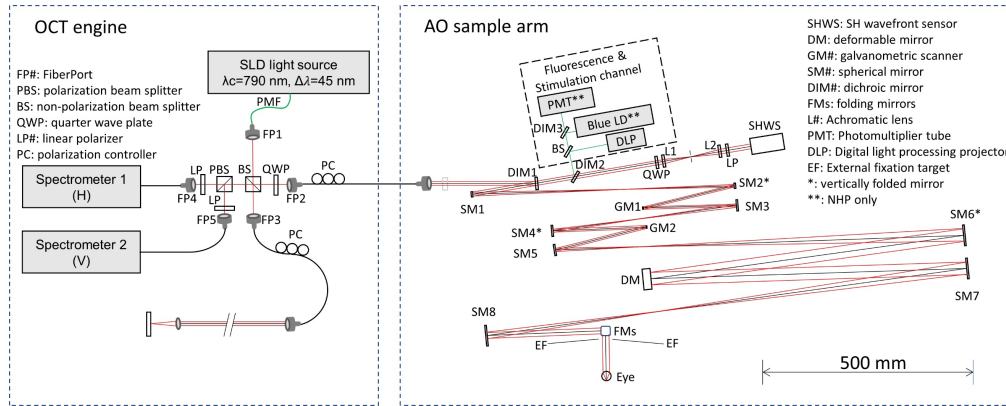


Fig. 2. Schematic diagram of multifunctional AO-OCT system. (left) OCT engine and (right) AO sample arm with a stimulation channel. Of note, the same system design is used to build another duplicated machine for on-going studies in non-human primates, which includes a fluorescence channel (more details are described in Supplemental Section S1.3 for interested readers).

Table 1. Key system parameters

| | |
|----------------------------------------|------------------------------------------------|
| Imaging beam wavelength | 790 nm \pm 22 nm |
| Imaging beam power incident on the eye | \sim 400 μ W |
| Imaging beam size on the eye | 7.1 mm |
| Lateral resolution | 2.3 μ m |
| Axial resolution | 4.5 μ m in tissue ($n=1.38$) |
| Field of view | Up to 2.8° (H) \times 2.8° (V) |
| AO-OCT A-line scan rate | 250,000 A-lines/s |

2.2 Software

We developed 1) real-time control software to operate the multifunctional AO-OCT imaging system and 2) offline postprocessing software to register and average hundreds of AO-OCT volumes images to compute reflectance, retardance, optic axis orientation, and angiogram.

2.2.1 Real-time control software

The in-house control software manages OCT and AO subsystems independently and concurrently. The OCT control software continuously acquires the AO-OCT volume images by scanning the sample tissue. In parallel, the AO control software dynamically corrects for measured monochromatic aberrations to improve image quality. Their respective graphic user interfaces (GUIs) allow for real-time monitoring, recording, and on-the-fly parameter change, all with minimum delay, allowing consistent and flexible operation during imaging experiments. Of note, some of the foundational components of our code (signal generation, center of gravity computation, and pixel displacement algorithms) were originally developed by Miller's Lab at Indiana University School of Optometry; however, our software rapidly evolved to meet our unique needs. Specific instances are detailed within the [Supplemental Section S2](#).

2.2.2 Offline processing software

Hundreds of AO-OCT volume images were reconstructed, registered, and averaged after each experiment to improve the contrast. We used the previously developed algorithms [67,73–75] but with significant modifications in order to incorporate two orthogonal, complex-numbered,

A-line scans $A_H(z)$ (H channel) and $A_V(z)$ (V channel) acquired by the polarization diversity detection channel. We computed the temporally-averaged reflectance $A(z)$, retardance $\delta(z)$, optic axis orientation $\theta(z)$, and angiogram $D(z)$ for a given A-line scan registered to a global coordinate [67] using the following equations:

$$A(z) = \frac{1}{N} \sum_i \sqrt{A_{H,i}^2(z) + A_{V,i}^2(z)}, \quad (1)$$

$$\delta(z) = \tan^{-1} \left(\frac{\sum_i |A_{V,i}(z)|}{\sum_i |A_{H,i}(z)|} \right), \quad (2)$$

$$\theta(z) = -\frac{1}{2} \cdot \angle \left[\exp \left\{ i \cdot \left(\angle \left(\sum_i \frac{A_{V,i}(z)}{A_{H,i}(z)} \right) - 2\theta_c \right) \right\} \right], \quad (3)$$

$$D(z) = \frac{1}{N-1} \sum_i \left| \frac{A_i(z) - A_{i+1}(z)}{A_i(z) + A_{i+1}(z)} \right|, \quad (4)$$

where $A(z)$ is the averaged normalized amplitude reflectance, $\delta(z)$ is the average retardance, $\theta(z)$ is the average optic axis orientation, $D(z)$ is the average amplitude difference, i is the registered volume index, and N is the total number of registered A-line scans. Note that the phase offset, θ_c , is arbitrary in our system (see [Supplemental Subsection S1.1](#)), but we forcibly set $\theta_c = 0$ to test the measurement accuracy and repeatability unless otherwise specified.

2.3 AO-OCT imaging protocol

Table 2 summarizes imaging parameters used for testing the imaging performance of multifunctional AO-OCT system in a model eye and three healthy subjects. We scanned the sample object or human retina over $1^\circ \times 1^\circ$ FOV with A-line spatial sampling of 256×256 at A-line scan speed of 250,000 Hz. AO-OCT volumes were collected at a rate of 3.8 volumes/sec.

The human imaging protocol is described as follows. We first instilled an eye drop (Tropicamide 0.5%) for pupil dilation to allow higher-quality imaging. We waited 20 minutes to fully dilate the pupil and start the AO-OCT imaging session. During an imaging experiment, the subject sat and looked into the imaging instrument, like the standard clinical OCT instrument. The technicians controlled the subject's head position via the motorized stage and hand controller ([Supplemental Subsection S1.4](#)) by monitoring the pupil position and retinal depth displayed on the GUIs ([Supplemental Subsection S2.2](#)). Then, the subject was asked to keep the eye open and look steadily at a fixation target while holding a steady head position on the chin rest during each 4-second video. We repeated this live video acquisition ten times for each location or focus. The imaging session took about 1 hour, with enough time for breaks to mitigate fatigue and discomfort. We conducted the imaging experiment for the specially targeted locations in the eye: the central and peripheral ONH, the peripapillary RFNL, and the Bjerrum region along an arcuate RNFB path. At each location, we reconstructed three-dimensional volumetric images of AO-OCT-based reflectance, retardance, optic axis orientation, and angiogram by averaging more than a hundred volume images registered to a global coordinate system (see [Subsection 2.2.2](#)). All procedures adhered to the tenets of the Declaration of Helsinki and were approved by the Legacy Health Institutional Review Board. Written informed consent was obtained from all subjects before the experiment.

Table 2. AO-OCT imaging parameters

| | |
|------------------------------|--------------------------------------------|
| AO-OCT A-line sampling rate | 256 (H) \times 256 (V) A-lines/ $^\circ$ |
| AO-OCT imaging field of view | 1° (H) \times 1° (V) |
| AO-OCT volume rate | 3.8 volumes/second |

3. Results

We describe results in two sections: Section 3.1 describes the experimental results of characterizing and assessing the imaging performance of newly developed multifunctional AO-OCT tested in a model eye. Section 3.2 describes the AO-OCT imaging results tested in three healthy subjects from our ongoing feasibility study that aimed to establish a range of parameter variability in the normative database.

3.1 Optical system performance

We tested the AO-OCT imaging performance using a model eye consisting of a sample object, iris, and achromatic lens with a focal length of either 30mm or 75mm. We first assessed the AO-OCT imaging resolution (see [Figs. 3 \(a\) and \(b\)](#)). Then, we characterized the AO-OCT reflectance, retardance, and optic axis orientation measurements using a Scotch transparent tape as a sample (see [Figs. 3 \(c\)-\(e\)](#)).

The lateral resolution was assessed using the USAF 1951 test target printed on heavy white paper (RES-2; Newport) as the sample object. We chose this highly scattering sample as a resolution target to better emulate a retinal imaging scenario, e.g., the precise focusing control with AO to maximize image sharpness. We used the image detected by the V channel, containing mostly randomly polarized diffuse components of the light from the highly scattering media; because strong specular surface reflections detected by the H channel obscure the printed pattern. [Figure 3 \(a\)](#) shows the test target pattern imaged by the V-channel. The pattern was clearly visible with minimum distortion toward the edge. Using Gaussian fit and the objective lens with the focal length of 30mm, we found a $1/e^2$ beam waist spot radius of 2.8 μm as shown in [Fig. 3 \(b\)](#), approximately 30% larger than expected, presumably due to the multiply scattering effect. We further discuss this assessment in [Supplemental Section S3](#). We also assessed the axial resolution (FWHM) in the intensity scale using a specular reflection from the mirror surface with protective silver coating, which was 5.8 μm in tissue (refractive index = 1.38), 30% larger than expected but within the range of the previously reported number with the same light source [76].

Next, we measured the AO-OCT reflectance, retardance, and optic axis orientation of Scotch transparent tape (600 series; 3M) by repeatedly scanning the same location. We then computed mean reflectance, mean retardance and mean optic axis by averaging 256 B-scan images. The AO-OCT imaging beam focus was shifted toward the achromatic lens (focal length = 75mm) to avoid a strong specular reflection from the glossy surface and transmit more light into the roll tape (-1.7D). [Figure 3 \(c\)](#) shows temporally averaged cross-sectional B-scan images of the normalized amplitude reflectance, the retardance, and the optic axis orientation. The axial profile of normalized amplitude reflectance is shown in [Fig. 3 \(d\)](#). Mean amplitude reflectance from the adhesive-film interface was approximately 0.17%, uniform across the depths down to 2.0mm (refractive index of 1.5) after the normalization and the correction for the sensitivity roll-off (see [Supplemental Section S1.1](#)). The axial profiles of retardance and optic axis orientation in [Fig. 3 \(e\)](#) show a triangular and binary pattern, respectively, demonstrating the feasibility of depth-resolved polarimetry. However, they also show the consequence of inevitable phase ambiguity in measuring single-pass sample retardance larger than a quarter wave.

Given that the roll tape consisted of multilayered birefringent films, each having the same optic axis, the measured retardance should increase linearly, whereas the optic axis orientation remains constant. However, the phase ambiguity caused the retardance's negative slope and abrupt 90° rotation of the optic axis systematically and periodically, as shown in [Fig. 3 \(e\)](#). To account for this inevitable phase ambiguity, we adopted a simple theoretical model in which the retardance takes the form of a triangular waveform while the optic axis orientation exhibits a square waveform. As predicted, the measured retardances were nicely fitted to the theoretical

triangular waveform with the RMS error of 10° . The measured optic axis orientations were fitted to the theoretical square waveform with the RMS error of 29° (after removing unreliable data points where the retardance $< 20^\circ$ or the retardance $> 70^\circ$). This poor performance was primarily due to the presence of “frozen” speckles. Indeed, in another experiment where we used a Berek compensator and a reflective mirror, we achieved substantially better performance; the RMS error was 3° for both retardance and optic axis orientation measurements. These results indicate the vital need for a speckle reduction technique in most stationary biological tissues. As a matter of fact, it's common to apply the spatial averaging of neighboring speckles in polarization-sensitive OCT measurements at the expense of resolution.

Finally, we estimated the film birefringence by accounting the proportion of backing material (65.5%) to the whole layer thickness. The estimated birefringence was 0.0012, within the literature value range (0.0007-0.0022) [77,78], although this can be dependent on environmental factors such as mechanical stress and temperature.

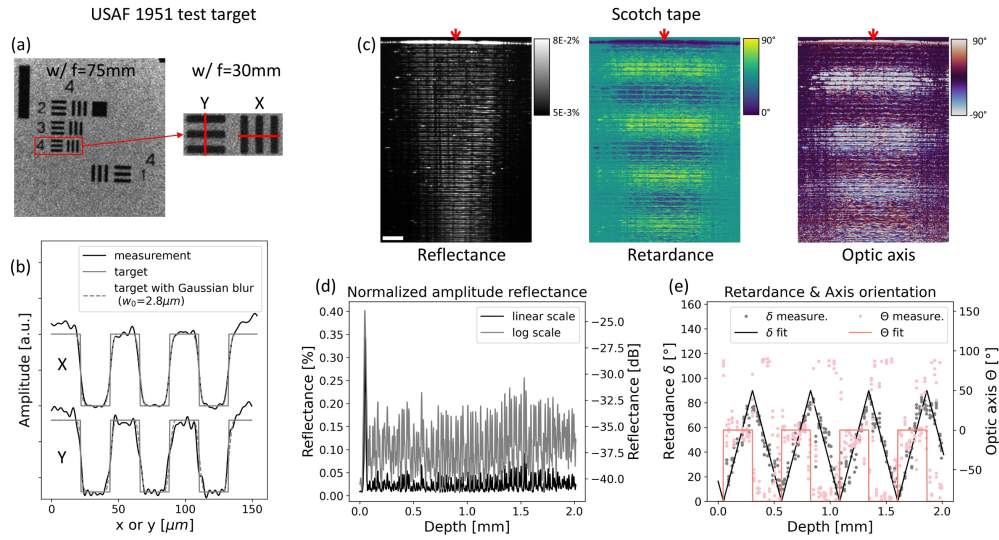


Fig. 3. Characterizing the imaging resolution (a), (b), and the reflectance, retardance, and optic axis orientation measurements (c) of the multifunctional AO-OCT. (a) *En-face* images of a USAF 1951 test target with a lens focal length of 75mm (left) and 30mm (right), respectively. The red lines, labeled with "X" and "Y," denote the positions of the amplitude profiles shown in (b). We found a $1/e^2$ beam waist spot radius of $2.8 \mu\text{m}$ using Gaussian fitting. (c) Cross-sectional images of Scotch tape corresponding to AO-OCT reflectance (left), retardance (middle), and optic axis orientation (right). (d) shows the normalized amplitude reflectance up to 2.0mm (refractive index of 1.5) along the axial scan position denoted by the red arrow in c (left) as a function of scan depth. (e) shows the single-pass cumulative phase retardation and optic axis orientation up to 2.0mm along the axial scan position denoted by the red arrow in c (middle and right). The white bar denotes $200 \mu\text{m}$.

3.2 *In vivo* human imaging performance

We characterized the AO-OCT imaging performance in three healthy human subjects by systematically and longitudinally surveying select fundus locations, including ONH, arcuate (Bjerrum) regions, and macula. Table 3 summarizes the subject information.

Figure 4 shows representative AO-OCT imaging results at the specifically targeted locations in Subject H001 as follows: the peripapillary RNFL at locations (1-5) denoted by the green circled numbers, the ONH at location (0) denoted by the red circled number, and the arcuate RNFs at the locations (4, 6-8) denoted by the blue circled numbers. In the following subsections, we separately describe our observations, respectively.

Table 3. Subject information

| | Age | Male/Female | Refraction |
|------|--------|-------------|------------|
| H001 | 37 y/o | M | -7D |
| H002 | 36 y/o | F | -2D |
| H003 | 57 y/o | M | +2D |

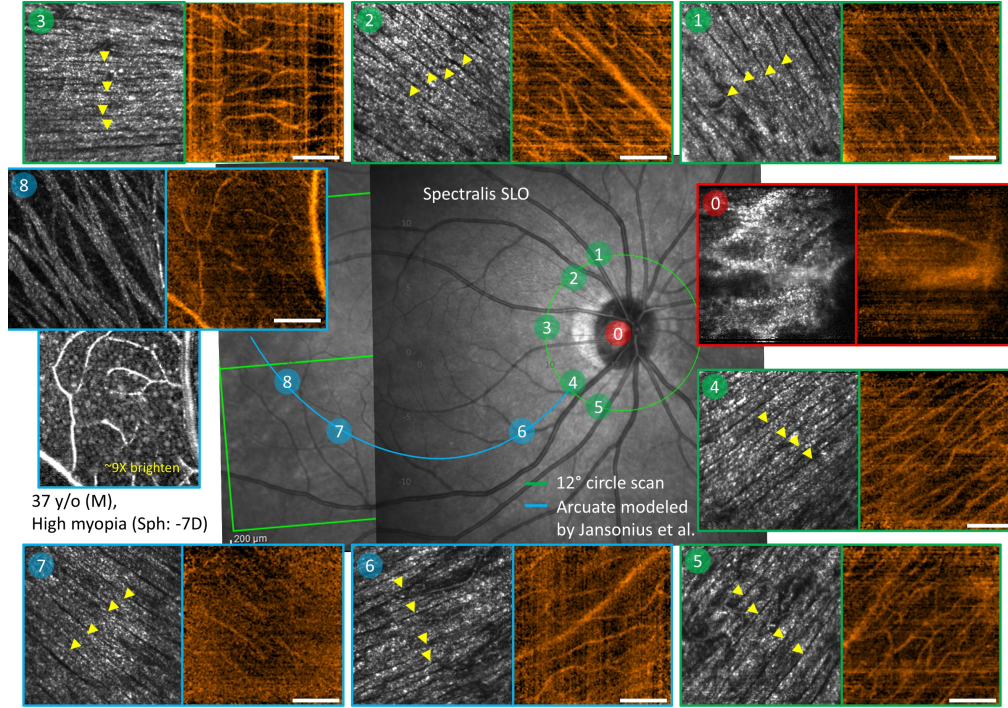


Fig. 4. Collage of *en-face* image pairs, each showing multifunctional AO-OCT reflectance (left) and angiogram (right), captured from the right eye of a 37 y/o subject with high myopia (Sph: -7D; H001) at circled numbered positions in the Spectralis SLO image. (0) Central ONH (see [Section 3.2.2](#)). (1-5) Radial striation patterns of Müller septa are visible with a width as narrow as a couple of micrometers as denoted by the yellow arrowheads, well aligned with peripapillary radial capillaries in the corresponding angiogram (see [Section 3.2.1](#)). (6-8) The RNFBs continue to extend toward the temporal retina along the arcuate as predicted by Jansonius et al.'s model [79] (see [Section 3.2.3](#)). At location (8), the individual GCL somas are visible by adjusting the image brightness (9X brighter). The white bars denote 100 μm . The angiograms were bandpass filtered to improve the contrast.

3.2.1 Peripapillary RNFBs, Müller septa, and radial capillaries

Peripapillary RNFL (pRNFL) thickness is a prominent structural measure for glaucoma [6,7,9–11] and other neurodegenerative diseases [8]. recent attention focuses on the peripapillary vasculature (peripapillary radial capillaries; PRCs) [46] as well as pRNFL reflectance [47–49] and retardance (or birefringence) [50,52]. Here, we measured the pRNFL reflectance, angiogram, retardance, and optic axis orientation at the selected locations (1-5) in [Fig. 4](#), the temporal side of the peripapillary region with the 3.5mm circle around the ONH. We systematically controlled the focus position to cover the full thickness of pRNFL. We go over our gross measurement of pRNFL, parameterization of pRNFL measurements, and repeatability assessments of pRNFL measurement in the following subsections.

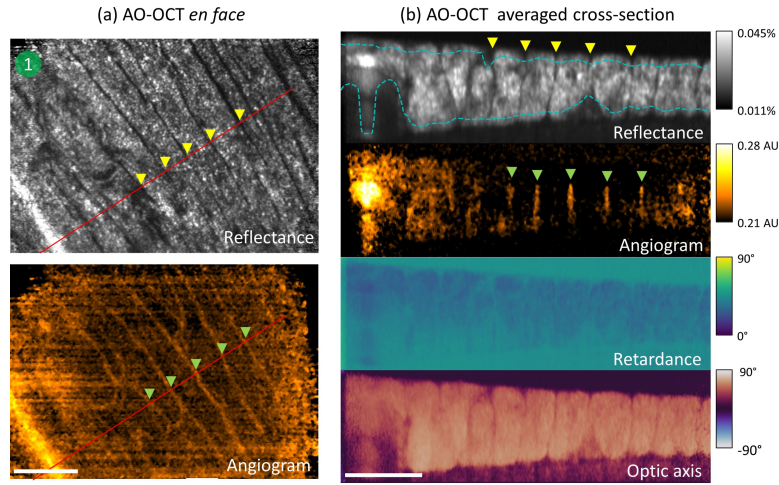


Fig. 5 Representative AO-OCT imaging results of peripapillary RNFL reflectance, angiogram, retardance, and optic axis orientation in the right eye of 37 y/o subject with high myopia (Sph: -7D; H001) at location 1 (see Fig. 4). (a) En face image pair of reflectance (left) and angiogram (right). (b) Cross-sectional images of reflectance, angiogram, retardance, and optic axis orientation along the red line as denoted in (a). Twenty cross-sectional images (25 μm) were averaged along the direction perpendicular to the RNF orientation to reduce speckle noise while maintaining its parallel structure. The yellow and green arrowheads denote the positions of individual Müller septa and PRCs, respectively. The blue dashed curved lines denote the automatically segmented anterior and posterior surface of the pRNFL. The white bars denote 100 μm. The angiograms were bandpass filtered to improve the contrast.

3.2.1.1 Gross measurement of pRNFL

Figure 5 shows the representative imaging results of the pRNFL at location 1 (see Fig. 4). The AO-OCT reflectance volume image revealed stunning details of individual pRNFBs surrounded by Müller cell processes that form radially oriented sheet-like columns as indicated by the yellow arrowheads (see Figs. 5 (a) and (b)). We know that the darker partitions of the striation pattern seen via ophthalmoscope is likely corresponding to the broadened foot endings of Müller cells near the retinal anterior surface [80]. Indeed, the darker partitions of the radial striation pattern seen by the AO-OCT (see Fig. 5 (a)) continue into the depth, forming sheet-like columns, and splitting the pRNFBs as predicted (see Fig. 5 (b) top). We therefore used this striation pattern to quantify peripapillary Müller cell process spacings. In addition, the AO-OCT angiogram nicely resolved the individual PRCs within the pRNFL despite the low contrast due to the coarse spatial sampling as indicated by the green arrowheads (see Figs. 5 (a) and (b)). The PRCs were otherwise not discernable from the corresponding reflectance image, unlike other capillaries in intermediate and deep capillary plexus. At this location, the PRCs formed a monolayer plexus, resided within each pRNFB, and did not coincide with the darker partitions. Later, we quantified PRC density and nearest-neighbor spacing by identifying individual PRC coordinates in each angiogram cross section. The blue dashed curved lines shown in the reflectance cross-section (Fig. 5(b) top) correspond to the automatically segmented anterior and posterior surfaces of the pRNFL from which we computed the pRNFL thickness. Unlike the most common approach delineating the edges of pRNFL surfaces, we used the pRNFL reflectance peak positions to avoid scaling bias (e.g., linear or log scale); therefore, our pRNFL thickness measurements could be more robust against systematic change, including a change in the point spread function, but likely underestimated compared to the normal range established in clinical OCT. In this study, we made no attempt to perform a direct comparison, but instead used the approach to measure the pRNFL thickness. Lastly, we measured the AO-OCT retardance and optic axis of the pRNFBs to characterize the well-being of fiber parallel structure, density, and orientation (Fig. 5 (b) bottom two rows). Their

corresponding cross-sections illustrate the cumulative nature of the OCT-based polarimetry as the beam traverses into the tissue. The retardance and optic axis orientation were elevated at the anterior surface of the retina due to the combined effect of the corneal birefringence, the SMF-based rotator, and some residual errors. Later, we corrected for these systematic effects using the surface Jones matrix [81,82] and quantified the pRNFL local birefringence and local optic axis orientation.

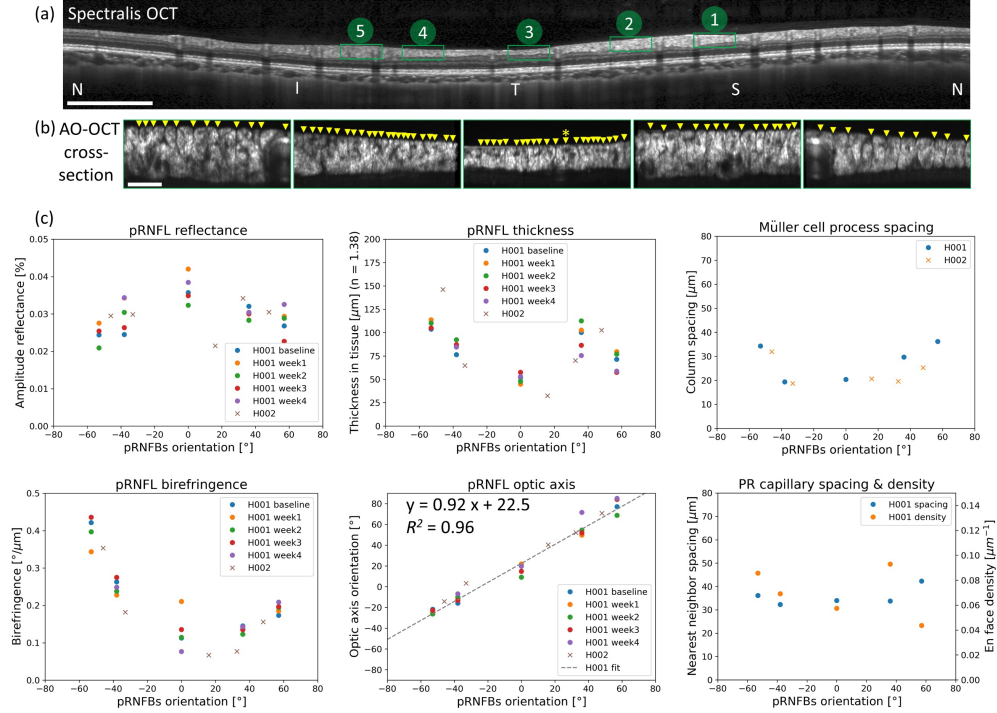


Figure 6. Measurements of peripapillary RNFL reflectance, thickness, birefringence, optic axis, Müller cell process spacing, PR capillary density/spacing in two healthy subjects (H001 and H002). (a) Spectralis 12° circle scan. The green boxes denote the AO-OCT imaging locations. (b) AO-OCT cross-sectional image for each location. The yellow arrowheads denote the manually identified Müller septa. The star indicates the septum aligned with the capillary. (c) pRNFL reflectance, thickness, birefringence, optic axis, and Müller cell process spacing are plotted against the manually determined pRNFBs orientation from the AO-OCT reflectance volume.

3.2.1.2 Parametrizing pRNFL measurements

Figure 6 summarizes the pRNFL thickness, reflectance, birefringence, optic axis orientation, Müller cell process spacing, and PRC spacing/density measurements of two healthy subjects (37 years old subject with high myopia (H001) and 36 years old subject (H002)) from our ongoing study, plotted against the pRNFBs orientation respective to the horizontal scan axis of AO-OCT imaging instrument. For comparison, we used the entire field of view instead of the overlap area to analyze the pRNFL properties at each location. The pRNFL reflectance from the anterior surface of the pRNFL varied across the locations in both subjects, albeit in distinct patterns between the two subjects, i.e., the reflectance at the papillomacular region was the strongest in H001 but the weakest in H002 (see **Fig. 6 (c) top left**). The pRNFL thickness appeared to follow the well-known double-hump pattern [83] (see **Fig. 6 (c) top middle**). The thickness measurement was more stable (coefficient of variance (COV) = 10%) compared to the pRNFL reflectance (COV = 12%), but the difference was small. The inclusion of large blood vessels contributed the most to the thickness measurement variability (see **Fig. 5 (b) top**),

which was more significant in the superior regions (locations 1 and 2). The Müller cell process spacings (see Fig. 6 (c) top right) were within the range of a histology report [84] and denser toward the papillomacular region in both subjects. Although not all Müller cell processes were traceable in their cross-sectional images (see Fig. 6 (b)), their conical expansion near the inner limiting membrane allows us to identify each septum. The PR capillary density in H001 was the most correlated with their corresponding pRNFL thickness, consistent with the previous report [85] (see Fig. 6 (c) bottom right). However, the cross-sectional nearest-neighbor PR capillary spacings resolved by the AO-OCT angiogram were relatively flat across the locations, indicating a regular distribution of PRCs within pRNFL to support their neighbor unmyelinated energy-demanding axons. The PRC in H002 was not well resolved due to its low contrast.

The pRNFL local birefringence and optic axis orientations were computed after correcting for the surface Jones matrix with an assumption that the RNFB have the same optic axis throughout its depth [82] (see Figs. 6 (c) bottom left and middle). The pRNFL birefringence in both subjects shows an intriguing quadratic pattern similar to Müller cell process spacing rather than the double-hump pattern of the pRNFL thickness. Also, we found the pRNFL birefringence was the most variable in the papillomacular region in H001, presumably due to larger regional variability. The pRNFL birefringence in both subjects ($0.22^\circ \pm 0.12^\circ$ in H001; $0.17^\circ \pm 0.12^\circ$ in H002) was larger or near the upper limit of the previous reports [86–90,52]. The higher birefringence in H001 is intriguing as it could reflect the stretched nerve fibers in high myopia [91]. The measured pRNFL optic axis orientations were strongly correlated with the manually determined pRNFBs orientation ($R^2 = 0.96$) in subject H001. The slope of the fitted line, 0.92, was close to 1. The offset was 22.5° , consistent across the measurements. In subject H002, the measured pRNFL optic axis orientations nicely followed the fitted line and were within the prediction interval of H001 measurements.

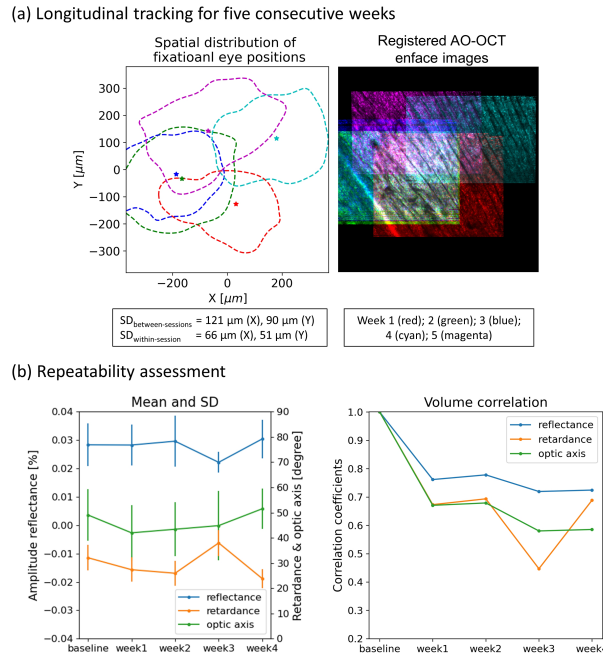


Figure 7. Repeatability test results of peripapillary RNFL measurements at location (1) in the right eye of a well-trained subject (H001). (a) The impact of involuntary eye motions on the pRNFL imaging for five consecutive weeks. The image on the left merges the five AO-OCT en face images, each color-coded by the week, i.e., baseline (red), week 1 (green), week 2 (blue); week 3 (cyan), and week 4 (magenta), respectively. The corresponding spatial distributions of the eye positions tracked by our software are shown on the right. The color-coded stars denote the mean positions of the eye motion trace. The color-coded isoline contours encompass 3SDs

of the eye motion trace. (b) The repeatability test results of the reflectance, retardance, and optic axis orientation measurements on the anterior surface of the pRNFL within the overlap area. The means and SDs of each measure are shown on the left. Their volume correlation coefficients are shown on the right.

3.2.1.3 Assessing repeatability of pRNFL measurements

We assessed the repeatability of our AO-OCT measurements in a well-trained, healthy subject (H001). We measured the same selected patches at locations (1-5) in [Fig. 4](#) by directing the subject to fixate on each corresponding LED target during a weekly imaging session done for five consecutive weeks. A major challenge was involuntary eye movements, as depicted in [Fig. 7 \(a\)](#). The mean positions of the eye motion trace varied significantly (One-way ANOVA, $p < 0.001$). The standard deviations (SDs) of the mean horizontal and vertical positions were 121 μm and 90 μm , respectively. Consequently, the overlap area progressively diminished over the course of the weeks, reducing to $0.6^\circ \times 0.4^\circ$, about 25% of the initial scan area ($1^\circ \times 1^\circ$). Nonetheless, we were able to track and measure the same patch for five consecutive weeks, where we measured means, SDs, and autocorrelations of AO-OCT reflectance, retardance, and optic axis orientation, respectively. The mean and SD of each measure were computed at the anterior surface of the pRNFL ([Figs. 7 \(b\) left](#)). The reflectance, retardance, and optics axis volumes were correlated with their respective baseline volumes ([Figs. 7 \(b\) right](#)). Overall, the measured reflectance, retardance, and optic axis orientations were $0.026 \pm 0.007\%$, $29.4 \pm 4.8^\circ$, and $46 \pm 11^\circ$, respectively. The mean values for each measure were similar over the course of measurements, and their volume images were moderately correlated with the baseline except the retardance in week 3 (see next paragraph for the details). These results indicate their stable performance. In contrast, their absolute measurements were more challenging. The converted intensity reflectance in the log scale was -72dB, only a few dB weaker than the lower limit of the previous estimate based on an OCT literature [12,92]. Both are, not surprisingly, significantly weaker than the predicted reflectivity from the Fresnel equation ($\sim -32\text{dB}$) as a consequence of diffuse scattering and coherent detection. The retardance and optic axis at the anterior of the pRNFL which represents the combined effect of the corneal birefringence, the SMF rotator, and some residual errors, were within a normal range of the previous report of corneal retardance and optic axis [93], but not surprisingly, the measured optic axis was rotated by a certain amount as described in the following paragraphs. We found the overall tendency was the same across all the patches we examined (see [Fig. S4](#)).

Of note, we found a relatively low reflectance and high retardance as well as a substantial drop in the volume correlation of retardance in week 3 due to the subtle misalignment in the bulk interferometer. After the realignment in week 4, the overall reflectance and retardance came back to the normal range, but there was a systematic rotation of the optic axis. So, we numerically corrected for the rotation by setting the phase offset in [Eq. \(3\)](#) as $\theta_c = 22.5^\circ$ in week 4. Since then, the system has demonstrated robust performance. In addition, regardless of the misalignment in week 3, pRNFL local birefringence and local optic axis measurements were measurable and consistent across weeks after correcting for surface Jones matrix (see [Subsection 3.2.1.2](#) and [Fig. 6](#)), suggesting that any systematic change, including temperature change and mechanical stress, was numerically canceled.

3.2.2. Prelaminar and laminar regions within the central ONH

We know of the characteristic damage to the ONH in normal aging, glaucoma [53–59], and other neurodegenerative diseases [8]. Discerning ONH tissue microstructures, their deformation and remodeling, including reactive gliosis and fibrosis, is central to further understanding of underlying pathophysiology [53,61]. Using the multifunctional AO-OCT, we imaged the central ONH in two healthy subjects (H001 and H003) with relatively thinner prelaminar tissue above the LC. We go over our process of optimizing the ONH imaging method, detailed observation of central ONH, and other ONH imaging results in the following subsections.

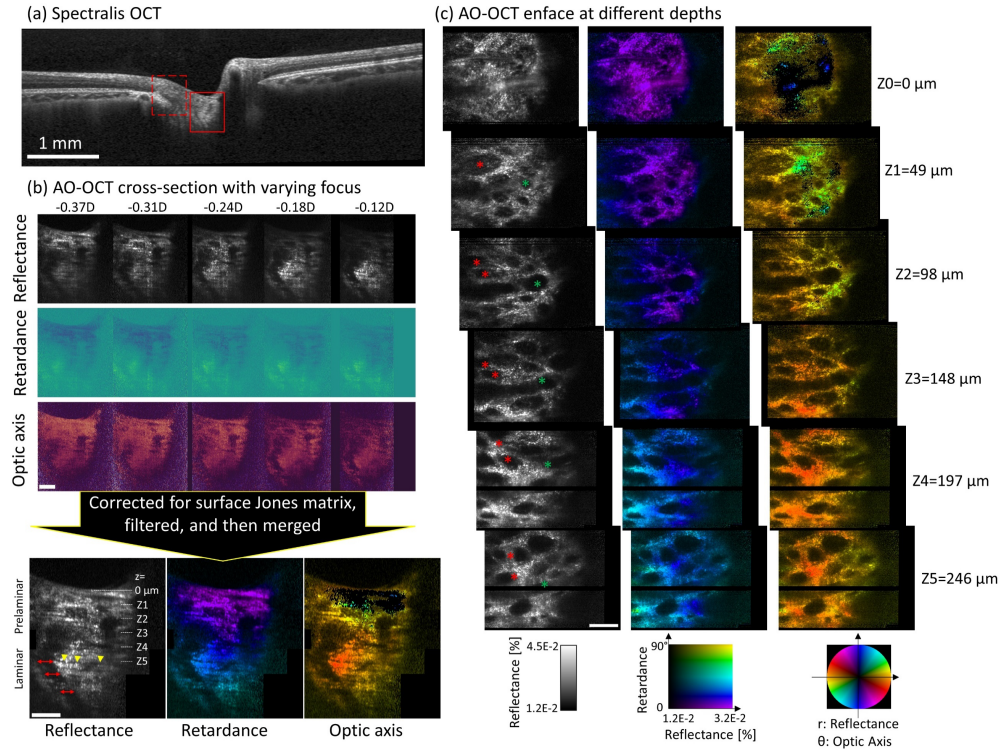


Figure 8. Multifunctional AO-OCT reflectometry and polarimetry reveal the detailed view of prelamina and lamina tissue in a 37 y/o subject with high myopia. (a) Spectralis OCT image with 1:1 aspect ratio. The red square denotes the corresponding cross-sectional area imaged by the multifunctional AO-OCT. The red dashed-line square denotes the corresponding area image (see [Supplemental Section S4](#) and [Fig. S5](#)). (b) Cross sections of AO-OCT reflectance, retardance, and optic axis with varying focus. The color change in the retardance and optic axis images represents their value change, which follows the color maps shown on the bottom right. The red arrows denote the width of dark trunk-like structures in the lamina cribrosa (aka LC pore); however, the width varies significantly depending on which cross-section is used. The striation pattern is visible in the lamina region and, to a lesser extent in the prelamina region (see also [Visualization 1](#)). The yellow arrowheads denote one of the dark partitions that continues across the entire FOV. (c) En-face images of AO-OCT reflectance, retardance, and optic axis orientation at different depths (Z0, Z1, ..., Z5). The green and red asterisks denote the axon bundle's center positions, illustrating a tortuous path through the prelamina and lamina regions. We mask out unreliable pixels of optic axis orientation with a retardance smaller than 5° . The white bars denote $100 \mu\text{m}$ unless otherwise specified.

3.2.2.1 Optimizing ONH measurement

Figure 8 shows a detailed view of the extremely complicated structure of the central ONH in H001 resolved by the newly developed multifunctional AO-OCT. To fully reconstruct the entire volume across the depths, we systematically controlled the focus position by adding a certain defocus amount to the reference wavefront from -0.37D to -0.12D with a step of 0.06D . The reflectance at their corresponding depths became brighter and sharper as the focus altered, as shown in [Figure 8 \(b\)](#). In contrast, the retardance and optic axis orientation didn't change their contrast by focusing, except in the low SNR region, suggesting a negligible effect of focusing on the AO-OCT retardance and optic axis orientation measurement. We, therefore, merged all the in-focus volume images into one via focus stacking combined with a simple affine transformation. The detailed method was described in [67] but with modifications as follows. We instead simply averaged all the volumes, averaged the volumes with the focus at the same depth, and then extracted an in-focus subvolume from the averaged volume with the

thickness approximately same as the depth of focus ($\sim 50\mu\text{m}$) by finding an approximated plane of best focus. Then, we iterated this over step focuses, made a set of subvolumes with different focuses, and registered and mapped them onto the same coordinate. By doing so, we kept all depths in focus. Indeed, the reflectance cross-sectional image shows nearly equal brightness across the entire depth similar to corresponding Spectralis OCT image (see [Figure 8 \(b\) bottom](#)), and the enface images at different depths show sharply focused connective tissues within prelaminar and laminar regions, as shown in [Figure 8 \(c\)](#).

3.2.2.2 Detailed visualization of central ONH

In the surface nerve fiber region (at Z0 in [Fig. 8 \(c\)](#)), including the inner limiting membrane of Elschning, the speckles were formed by the reflections primarily from nerve fiber cytoskeletons, capillaries, and connective tissues, like those of the pRNFBs (see [Figs. 5 and 6](#)). However, as soon as the axon bundles turned nearly 90° toward the optic nerve (at around Z1), the reflected light from nerve fibers went off the pupil due to their strong directionality [94], and thus their bundles appeared as dark trunk-like structures (see [Visualization 1](#)). In contrast, the reflected light from the connective tissues remained back onto the pupil and appeared as a bright mesh-like network structure that continued across the depths and split the axon bundles. The tortuous paths of axon bundles (or dark trunk-like structures) were visible across prelaminar and laminar regions (see [Visualization 2](#)). We manually traced the center position of the same axon bundles across the depths, as denoted by the green and red asterisks in [Fig. 8 \(c\)](#). The tortuosity was higher at the preliminary region, and then the axon bundles were straightened in the laminar region. We also found that the axon bundle, denoted by the red asterisk, split into two within the preliminary region (from Z1 to Z2) by the bright connective tissue. The width of the individual axon bundles (or dark trunk-like structures) and beams (a bright mesh-like structure) varied significantly across the depths, particularly in the prelaminar regions (Z1-Z3). The reflectance of the bright connective tissues was uniform across the prelaminar and laminar regions, resulting in an indistinguishable boundary between the two regions, but varied across beams. In the cross-sectional images, the dark partitions of the striation pattern were visible and continued across the entire field of view primarily in the laminar region (Z4-Z6) (see [Visualization 1](#)). Histologically, astrocytes form several sheet-like structures perpendicular to axons, alternating with the laminar sheets of collagenous fibers along the depth [95,96]. Therefore, the periodic appearance of the dark partitions most likely corresponds to astrocytes (dark) and collagenous fibers (bright). Of note, the striation pattern is occasionally visible in clinical OCT, but we observed a substantially improved contrast in our AO-OCT owing to its resolution and motion correction accuracy.

The additional contrast provided by the AO-OCT polarimetry further detailed the ONH microstructure. The retardance and optic axis orientation volumes were reconstructed by applying a 3D Goldstein's phase filter ($\alpha = 0.2$) [97], correction for a surface Jones matrix [81], and focus stacking [67]. The cross-sectional retardance image shows dramatic color changes along the depth resulting from its cumulative effect, as shown in [Fig. 8 \(b\) bottom](#). The rate of retardance change in the depth increased progressively toward the laminar region and became the greatest in the laminar region, which is intriguing as it could indicate the difference in extracellular matrix composition. Histologically, we know 1. a progressive increase of collagenous fibrils is present towards the laminar region and 2. most elaborated network of collagenous fibers formed within the LC [96,98]. Indeed, we observed the greatest change of retardance occurred within the LC where the elaborated laminar beams and striated partitions were visible in our AO-OCT image. In addition, unlike peripapillary RNFBs, the effect of axon bundles could be safely ignored; because we confirmed most axon bundles were oriented approximately parallel to the beam by tracing the axon bundles (see [Visualizations 1 and 2](#)), further supporting the notion. Besides, the optic axis orientation measured by AO-OCT polarimetry could represent the collagenous fiber orientation, but its implication was difficult in the deeper regions because the optic axis orientation altered along

the depth (**Fig. 8 (b) bottom**). Thus, the direct visual inspection was very challenging unless the collagenous fibers were clearly exposed (see the next results). Nonetheless, the retardance and optic axis variation across laminar beams were visible, which could indicate the difference in extracellular matrix composition and mechanical stress/stretch (**Fig. 8 (c) Z4-Z6**). Lastly, the AO-OCT angiography located individual capillaries in the surface nerve fiber region which were critical in maintaining choked axon bundles as they turn 90 degrees, but not in the deeper regions due to its poor contrast to the surrounding tissue's pulsatile motion.

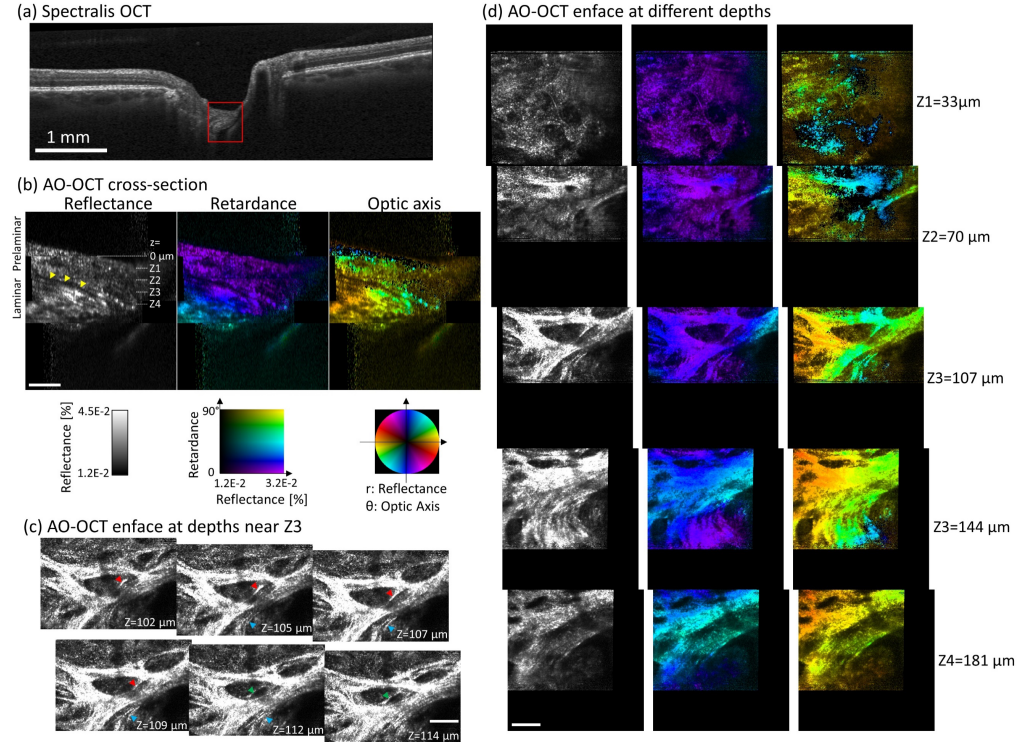


Fig. 9 Multifunctional AO-OCT reflectometry and polarimetry reveal the detailed view of prelamina and lamina tissue in a 57 y/o healthy subject with a relatively deep cup (H003). (a) Spectralis OCT image with 1:1 aspect ratio. The red square denotes the corresponding cross-sectional area imaged by the multifunctional AO-OCT. (b) Cross sections of AO-OCT reflectance, retardance, and optic axis orientation after the reconstruction. The color change in the retardance and optic axis images represents their value change, which follows the color maps shown on the bottom row. The yellow arrowheads denote one of the dark partitions that continues across the entire FOV. The periodic appearance of these dark partitions forming the striation pattern is more visible in the lamina region. (c) En-face images of AO-OCT reflectance at the depths near Z3, visualizing an intricate collagenous fiber network. The red, green, and blue arrowheads indicate isolated collagenous fiber bundles, respectively; some of them bridge the axon bundle and appear to be under-stressed/stretched (see also [Visualization 3](#)). (d) En-face images of AO-OCT reflectance, retardance, and optic axis orientation at different depths (Z1, Z2, ..., Z4). We mask out unreliable pixels with a retardance smaller than 5°. The white bars denote 100 μm unless otherwise specified.

3.2.2.3 Other ONH imaging results

Using the same methods established in Section 3.2.2.2, we found similar characteristic features in a 57 years old subject (H003; see **Fig. 9**), such as the transition of reflectance pattern of axon bundles near the surface retinal nerve fiber region (Z0); tortuous paths of the axon bundles across the depths; continuous structure of connective tissues (bright) splitting axons bundles (dark); and the striation pattern of astrocytes (dark) and collagenous fibers (bright) in the

laminar region (Z3-Z4). But we also observed some other distinct features. First, the laminar beams appeared more stretched. Even isolated collagenous fibers were visible, as indicated by the red, green, and blue arrowheads in [Fig. 9 \(c\)](#) (see also [Visualization 3](#)). Second, the reflections in the laminar regions (Z3-Z4) were approximately three times (in linear scale) brighter than those in the prelaminar regions (Z0-Z2), facilitating the boundary segmentation between the two. Third, the rate of retardance change (or birefringence) was higher than that of H001 in the LC. Fourth, the prelaminar tissue was thinner, exposing the collagenous fibers in the laminar region and easing the visual inspection of the optic axis orientation. Indeed, the optic axis orientations of the collagenous fibers appeared well aligned with manually determined collagenous fiber orientations, substantiating our polarimetry measurements (see [Fig. 9\(d\)](#)). The LC also appeared to be thinner, though we couldn't delineate the posterior boundary of LC due to the central retinal vasculature residing just underneath. These observations, such as stretched collagenous fibers, increased retardance within the LC, and thinner LC, may indicate tissue deformation and remodeling in response to mechanical stress or those related to the central retinal vasculature.

For further testing, we also measured the temporal ONH in H001 using the same methods described above (see [Supplemental Section S4, Fig. S5, Visualizations 4&5](#)).

3.2.3. Arcuate RNFBs and GCL somas:

Examining the region along an arcuate RNFL bundle could reveal the time course, sequence of pathophysiological events, and their correlations to established clinical manifestations (RNFL retardance loss and thinning, then capillary blood flow reduction) [62–66]. In addition, detecting the loss of the GCL soma in the living eye can establish the time course relative to other existing clinical metrics.

We imaged three additional patches along the arcuate in the Bjerrum region of H001 during the same imaging session with peripapillary RNFL imaging. We predetermined these targeted locations based on a mathematical prediction of the nerve fiber trace done by Jansson et al. [79] (see [Fig. 4](#)). The manually determined RNFBs' orientations were well-matched with the predicted fiber orientations. The optic axis orientation measurements were also well aligned but with an unknown offset of 22.5°, similar to those in the peripapillary RNFL measurements (see [Fig. 5](#)). We found the dispersed orientation of the RNFBs at location (8) near the temporal raphe consistent with histology [99]. The packed GCL somas were visible at the same location (8), and their reflectance was approximately 9X weaker than the RNFL reflectance in the linear intensity scale, consistent with the previous estimate based on an OCT literature [12,92]. The superior vascular complex (SVC) capillaries, including PRCs, were well aligned with the RNFB orientation near the ONH; however, the orientation and depth locations of the SVC capillaries dispersed toward the temporal raphe as expected.

4. Discussions

This manuscript describes and characterizes a new multifunctional AO-OCT system that measures reflectance, retardance, optic axis, and angiogram, all at the cellular scale in the living human retina and ONH. Rich structural information combined with the focus stacking and eye motion correction algorithms, enables a detailed view of the RNFBs, GCL somas, glial septa, capillaries, and connective tissues. These are key features of neurodegenerative diseases, including glaucoma. We discuss the significance and future perspectives of our multifunctional AO-OCT-based approaches in the following subsections.

4.1 AO-OCT reflectometry

AO-OCT-based reflectance is a fundamental measure for characterizing intrinsic optical properties of the living retina and ONH. Previous studies using AO-OCT have improved morphometry, i.e., measuring size, shape, orientation, and distribution of cellular features, such as RNFBs, GCL somas, and inner plexiform sublayers [21,22,100,18,37,101], which were not

easily discernible in clinical OCT. However, few attempts have been made to quantify the reflectance despite its significance in glaucoma [102,90,47–49], presumably due to its inherent variability. This variation is caused by several factors such as eye and head motion, blinking, opacity, effective numerical aperture (pupil size and axial length), and tissue directionality - as well as instrument errors, including coherent noise, polarization noise, and AO correction stability when including a focus control. We have attempted to address these issues by implementing 1) dedicated control software and a subject interface for seamless AO operation, including eye alignment; 2) the improved postprocessing methods of registering, normalizing, and averaging more than a hundred volume images; and 3) the polarization diversity detection to remove the impact of polarization artifacts in highly birefringent tissue [103]. We find our AO-OCT reflectometry is generally repeatable over time, reproducible across different locations and subjects, and free from polarization artifacts (see [Section 3.2](#)). Although some challenges likely remain to be seen, we anticipate that deploying the AO-OCT reflectometry and its morphometry will become essential for characterizing cellular and subcellular features in the living eye.

4.2 AO-OCT polarimetry

AO-OCT polarimetry is another excellent addition to conventional AO-OCT, which can measure the change in polarization properties of individual RNFBs and collagenous beams as indications of fiber loss, stress/stretch, deformation, and remodeling. Although Cense et al. previously demonstrated some of the potential of AO-OCT polarimetry [25], at that time, it was not possible to perform a full volume reconstruction with focus stacking and global image registration methods [67]. With the advancements we have made here, we successfully demonstrated the full volume reconstruction and substantially improved polarization measurement. We also made this possible with careful design and construction of our off-axis relay telescope and hybrid PS-OCT interferometer. Despite the initial concerns described below, we have successfully demonstrated the capability of AO-OCT polarimetry to measure retardance and optic axis orientation in the living human retina and ONH with excellent repeatability and reproducibility (see [Section 3.2](#)). The most significant concern when guaranteeing quantitative measurements is the signal-to-noise ratio (SNR) in PS-OCT measurement [104]. Indeed, the measured retardance and optic axis orientation both dramatically converge towards 45° and 0° , respectively, as the SNR reduces with increasing distance from the focus (see [Figs. 5 and 6](#)). Therefore, combining the in-focus volumes is necessary to fully reconstruct the retardance and optic axis volumes (see [Figs. 8, 9, and S5](#)). Our AO-OCT polarimetry results suggest a negligible impact of wavefront curvature in the weak birefringent tissue we measured. Thus, our simple approach of focus stacking could be justifiable, though a more sophisticated approach may improve the volume reconstruction. The speckle noise is a secondary yet significant concern (see [Section 3.1](#)). Typically, the spatial filter is applied to reduce the speckle noise at the expense of resolution. Thus, in non-AO PS-OCT measurements, multiple fiber bundles or laminar beams could be averaged out. The smaller speckle size in AO-OCT polarimetry allows the local averaging window to be small enough to resolve individual axon bundles and beams (see [Figs. 8, 9, and S5](#)), even isolated fiber bundles (see [Fig. 9 \(c\), \(d\) and Visualization 3](#)).

Another remaining challenge concerns the inherent limitations in the single-mode fiber-based PS-OCT. First, the optic axis measurement is relative because the single-mode optical fiber introduces an unknown phase offset (or rotation of the optic axis). Also, the state of optical fiber birefringence is sensitive to temperature change and mechanical force. Even if we corrected for the surface Jones matrix that includes such an error, theoretically, the true phase offset remains unknown [82]. Despite these concerns, we generally find excellent repeatability and reproducibility across intra-and inter-measurement sessions with a maneuver calibration prior to each measurement (see [Figs. 5 and S3](#)). For example, the measured optic axes strongly correlate with manually determined nerve fiber orientations but a “known” phase offset of 22.5°

(see Fig. 6). The exposed collagenous fiber orientation well aligns with the measured optic axis orientations after correcting for the surface Jones matrix (see Fig. 9 (c)). More encouragingly, without the correction for surface Jones matrix, the measured retardances and optic axes at the anterior surface (see Subsections 3.2.1) were aligned well with the previous report of corneal retardance and optic axis [93], even better if we accounted for the “known” phase offset of 22.5° found with the linear regression (see Fig. 6). Moreover, the numerical correction for the phase offset using Eq. 3 is required only after the realignment of the bulk interferometer over a series of experiments. These results show promise for an absolute optic axis measurement in future studies. Second, the cumulative nature of OCT-based polarimetry obstructs resolving local (or depth-resolved) birefringence and optic axis orientation. Although several numerical postprocessing approaches have been proposed for the local (or depth-resolved) analysis, absolutely accurate measurements and sophisticated numerical compensation are required to remove the numerical error propagating across the depths where the critical fiber components exist. For example, we need precise image segmentation to isolate the tissue with the same optic axis, inter/extrapolation to fill dark pixels, sophisticated noise reduction caused by shot noise, speckles, and multiply scattered light. Such a dedicated approach could be possible by combining our high-resolution AO-OCT images; however, it’s very time-consuming, requires some heuristic assumptions, and, more importantly, may not be necessary for detecting longitudinal changes of fiber loss, fibrosis, remodeling, and deformation.

4.3 AO-OCT angiography

AO-OCT angiography is a label-free imaging method that can measure individual capillary functionality through motion contrast, which was previously demonstrated for measuring retinal capillaries and choriocapillaris in macula [18,26–30], but not specifically PRCs in peripapillary region (see Subsection 3.2.1). Although we have limited use of AO-OCT angiography in the present study, its application is vast. The well-being of the superior vascular complex (SVC), including PRC, in peripapillary region has been extensively studied in glaucoma and other neurodegenerative diseases owing to its significant and unique role in supporting surrounding unmyelinated energy-demanding axons. The AO-OCT angiography can pave the way to resolve, locate, and quantify individual capillaries, their functionality, and their relation to surrounding tissue. Unlike the intermediate or deep capillary plexus, the PR capillaries are not easily discernible from the AO-OCT reflectance image due to the nearly equal reflectance from RNFBs (see Fig. 5). Thus, AO-OCT angiography is crucial in resolving and locating individual capillaries in SVC, particularly PRCs. Indeed, this study shows a promising use case of AO-OCT angiography for capillary morphometry (see Fig 6 (c)). Although the presented approach is not optimized for AO-OCT angiography, the denser sampling and modified scan protocol will further improve the contrast [27].

4.4 Implications of multifunctional imaging results

Most strikingly, the multifunctional imaging approach orchestrates the detailed view of the RNFBs, GCL somas, capillaries, glial septa, and connective tissues, key clinical features in neurodegenerative diseases, including glaucoma. For example, the peripapillary RNFBs are better visualized by averaging out the speckle noise along the axon axis measured by hand and by polarimetry (see Figs. 5 and 6). With the global image registration algorithm [67], this averaging method maintains the parallel structure of axons, Müller cell processes, and astrocytes and thus produces a high-quality, speckle-free, cross-sectional image of RNFBs and Müller septa. Indeed, the average cross-sectional image shows the intriguing heterogeneous reflectance pattern within each RNFB. The pattern is not solely attributed to the PR capillary reflections whose locations are identified via the angiogram, and thus, most likely reflecting the intra-bundle contents (axons and glial cells) and their distribution. Given that we also know of potential involvement of Müller cell in glaucoma [105], better visualizing Müller cell processes would help discern early manifestations of the disease. Now, we can test the effect

of axonal degeneration and gliosis on the intra-and inter-bundle reflectance pattern and their relation to capillary blood flow change, well-being of parallel axon structures, and RGC loss in living humans.

Another example is the ONH, one of the most challenging portions of the eye to be imaged by AO-OCT yet holding critical clinical features in glaucoma and other neurodegenerative diseases (see [Section 3.2.2](#)). The presence of large blood vessels, limited penetration, and considerable variability in ONH morphology across the subjects restrict the area or the number of subjects to be imaged and analyzed. Nonetheless, we have successfully imaged a portion of temporal and central ONH in two healthy subjects with relatively thinner prelaminar tissue. Combining focus stacking, global image registration, and volume composition algorithms allows a detailed view of ONH, almost resembling histological sections, with their polarization properties. With a deep understanding of histological features, we have shown promise to unravel complicated relationships of the intrinsic optical measures to the cellular and subcellular components and their distributions, including axon bundles, collagenous fibers, capillaries, and astrocytes, key clinical features in glaucoma and other neurodegenerative disease. We anticipate that further study will unravel the heterogeneous and interdependent relationship between the multifunctional AO-OCT-based measurements and manifestations of neurodegeneration, including neuronal loss, axonopathy, retinal gliosis, fibrosis, or vascular dysfunction. Particularly in glaucoma, the impact of mechanical stress on the ONH could be further investigated by directly or indirectly resolving degenerating axons, retinal gliosis, stressed/stretched collagenous fibers, and their remodeling together with capillary blood flow change and RGC loss, all in the living human eye.

4.5 Limitations and future perspectives

The limitations of the AO imaging are well documented elsewhere [106]. A major limitation, often unnecessarily exaggerated as the greatest barrier to translating AO into clinical practice, is the considerably smaller field of view and depth of focus, which could lead to longer measurement time and larger data size. To mitigate this, we have imaged specifically targeted locations of clinical interest, for example, the peripapillary retinal nerve fiber region, which is directly comparable with the current clinical measures. By doing so, we could use AO-OCT as a supplement, not a replacement, to current clinical tests so as to improve clinical assessment. Moreover, we simultaneously built a duplicate machine using the same system design for imaging non-human primates to accelerate “bench-to-bedside” discovery and vice versa, which includes histological validation, tests for a new drug or treatment, and evidence-based studies of underlying pathophysiology with well-controlled perturbations. It’s also worth mentioning that, in future studies, an additional fluorescence channel will allow for tracing specific markers, and a stimulation channel will be used for assessing neurovascular reactivity in response to various stimulus patterns. This translational approach with additional capabilities will further narrow down the targets, improving its efficiency while addressing scientific questions.

With that said, increasing the AO-OCT imaging speed is still highly demanding, particularly to reduce eye motion artifacts in patients with poor fixation. Although the MHz FDML source has made AO-OCT imaging much faster [107,108], it’s still limited to longer wavelength bands at the expense of resolution and scattering. A new swept-source development for an 800 nm wavelength band, which has the highest retinal imaging throughput [109], is awaited. High-speed AO would also be helpful as it could improve the imaging throughput [110]. Another important challenge is accurately tracking the same position over a long period. This study shows a very limited overlap area over five weeks, but we anticipate that this could be improved by increasing the display resolution. Indeed, our previous study showed a larger overlap possible with finer-pixel fixation display and its control in normal subjects [16–18] and a glaucomatous patient [111]. In the worst case, we could account for the effects of regional variability by finding a percent overlap.

5. Conclusion:

We demonstrated multifunctional imaging of the living human retina and ONH using a newly developed AO-OCT device that can measure reflectance, retardance, optic axis, and angiogram at the cellular scale. Multifunctional AO-OCT reveals astonishing details of RNFBs, GCL somas, capillaries, connective tissues, and glial septa in the living human eye. Although further studies are forthcoming, the preliminary results show promise in detecting key aspects of the disease and its progression at the cellular scale.

6. Funding

This study was supported by Good Samaritan Foundation, BrightFocus Foundation, and E. Matilda Ziegler Foundation for the Blind.

7. Acknowledgments

We thank Steven Mansberger, Brad Fortune, and Hongli Yang for fruitful discussions. We thank Cindy Albert and Clara Llorens-Quintana for data collection. We thank Juan Reynaud and Deepak Sapkota for their technical assistance. We thank Donald Miller, James Crowell, and Yan Liu at Indiana University for sharing source codes. We thank Yoshiaki Yasuno and Shuichi Makita at Tsukuba University and Masahiro Yamanari at Tomey Corporation for fruitful discussions regarding PS-OCT. We thank Good Samaritan Foundation for supporting this study. We thank BrightFocus Foundation for supporting to build a duplicate machine specifically designed for non-human primates. We thank E. Matilda Ziegler Foundation for support to build visual stimulation channels.

8. Disclosures

The authors declare no conflicts of interest.

9. Data availability statement

Data underlying the results presented in this paper are not publicly available at this time but may be obtained from the authors upon reasonable request.

Supplemental materials. See [Supplemental Document 1](#) and [Visualizations 1-5](#) for supporting content.

References

1. K. E. Thorpe, A. I. Levey, and J. Thomas, "U.S. BURDEN OF NEURODEGENERATIVE DISEASE," 13 (2021).
2. World Health Organization, *Global Action Plan on the Public Health Response to Dementia 2017–2025* (World Health Organization, 2017).
3. L. Wallace and C. Brayne, "The need for a better global dementia response," *The Lancet Neurology* **21**, 115–116 (2022).
4. L. K. Wareham, S. A. Liddelow, S. Temple, L. I. Benowitz, A. Di Polo, C. Wellington, J. L. Goldberg, Z. He, X. Duan, G. Bu, A. A. Davis, K. Shekhar, A. L. Torre, D. C. Chan, M. V. Canto-Soler, J. G. Flanagan, P. Subramanian, S. Rossi, T. Brunner, D. E. Bovenkamp, and D. J. Calkins, "Solving neurodegeneration: common mechanisms and strategies for new treatments," *Molecular Neurodegeneration* **17**, 23 (2022).
5. O. Hansson, "Biomarkers for neurodegenerative diseases," *Nat Med* **27**, 954–963 (2021).
6. I. I. Bussell, G. Wollstein, and J. S. Schuman, "OCT for glaucoma diagnosis, screening and detection of glaucoma progression," *Br J Ophthalmol* **98**, ii15–ii19 (2014).
7. B. Fortune, "In vivo imaging methods to assess glaucomatous optic neuropathy," *Experimental Eye Research* **141**, 139–153 (2015).
8. A. H. Kashani, S. Asanad, J. W. Chan, M. B. Singer, J. Zhang, M. Sharifi, M. M. Khansari, F. Abdolahi, Y. Shi, A. Biffi, H. Chui, and J. M. Ringman, "Past, present and future role of retinal imaging in neurodegenerative disease," *Progress in Retinal and Eye Research* **83**, 100938 (2021).
9. G. Beykin, A. M. Norcia, V. J. Srinivasan, A. Dubra, and J. L. Goldberg, "Discovery and clinical translation of novel glaucoma biomarkers," *Progress in Retinal and Eye Research* **80**, 100875 (2021).
10. A. Geevarghese, G. Wollstein, H. Ishikawa, and J. S. Schuman, "Optical Coherence Tomography and Glaucoma," *Annu. Rev. Vis. Sci.* (2021).

11. Y. Shiga, T. Nishida, J. W. Jeoung, A. Di Polo, and B. Fortune, "Optical coherence tomography and optical coherence tomography angiography: essential tools for detecting glaucoma and disease progression," *Frontiers in Ophthalmology* **3**, (2023).
12. D. T. Miller and K. Kurokawa, "Cellular-Scale Imaging of Transparent Retinal Structures and Processes Using Adaptive Optics Optical Coherence Tomography," *Annual Review of Vision Science* **6**, 115–148 (2020).
13. D. R. Williams, S. A. Burns, D. T. Miller, and A. Roorda, "Evolution of adaptive optics retinal imaging [Invited]," *Biomed. Opt. Express*, BOE **14**, 1307–1338 (2023).
14. M. Pircher and R. J. Zawadzki, "Combining adaptive optics with optical coherence tomography: unveiling the cellular structure of the human retina in vivo," *Expert Review of Ophthalmology* **2**, 1019–1035 (2007).
15. R. S. Jonnal, O. P. Kocaoglu, R. J. Zawadzki, Z. Liu, D. T. Miller, and J. S. Werner, "A Review of Adaptive Optics Optical Coherence Tomography: Technical Advances, Scientific Applications, and the Future," *Investigative Ophthalmology & Visual Science* **57**, OCT51 (2016).
16. K. Kurokawa, J. A. Crowell, F. Zhang, A. Lassoued, and D. T. Miller, "Measuring neuron loss in the retinal ganglion cell layer in healthy subjects," *Invest. Ophthalmol. Vis. Sci.* **60**, 1781–1781 (2019).
17. K. Kurokawa, F. Zhang, J. A. Crowell, A. Lassoued, and D. T. Miller, "Method to track and measure loss of inner retinal neurons in the living human eye," in *Ophthalmic Technologies XXIX* (International Society for Optics and Photonics, 2019), Vol. 10858, p. 108580L.
18. K. Kurokawa, J. A. Crowell, F. Zhang, and D. T. Miller, "Suite of methods for assessing inner retinal temporal dynamics across spatial and temporal scales in the living human eye," *NPh* **7**, 015013 (2020).
19. R. J. Zawadzki, B. Cense, Y. Zhang, S. S. Choi, D. T. Miller, and J. S. Werner, "Ultrahigh-resolution optical coherence tomography with monochromatic and chromatic aberration correction," *Opt. Express* **16**, 8126–8143 (2008).
20. C. Torti, B. Považay, B. Hofer, A. Unterhuber, J. Carroll, P. K. Ahnelt, and W. Drexler, "Adaptive optics optical coherence tomography at 120,000 depth scans/s for non-invasive cellular phenotyping of the living human retina," *Opt. Express*, OE **17**, 19382–19400 (2009).
21. O. P. Kocaoglu, B. Cense, R. S. Jonnal, Q. Wang, S. Lee, W. Gao, and D. T. Miller, "Imaging retinal nerve fiber bundles using optical coherence tomography with adaptive optics," *Vision Research* **51**, 1835–1844 (2011).
22. Z. Liu, K. Kurokawa, F. Zhang, J. J. Lee, and D. T. Miller, "Imaging and quantifying ganglion cells and other transparent neurons in the living human retina," *PNAS* **114**, 12803–12808 (2017).
23. Z. Nadler, B. Wang, J. S. Schuman, R. D. Ferguson, A. Patel, D. X. Hammer, R. A. Bilonick, H. Ishikawa, L. Kagemann, I. A. Sigal, and G. Wollstein, "In Vivo Three-Dimensional Characterization of the Healthy Human Lamina Cribrosa with Adaptive Optics Spectral-Domain Optical Coherence Tomography," *IOVS IOVS-14-15177* (2014).
24. Z. Nadler, B. Wang, G. Wollstein, J. E. Nevins, H. Ishikawa, R. Bilonick, L. Kagemann, I. A. Sigal, R. D. Ferguson, A. Patel, D. X. Hammer, and J. S. Schuman, "Repeatability of in vivo 3D lamina cribrosa microarchitecture using adaptive optics spectral domain optical coherence tomography," *Biomed. Opt. Express* **5**, 1114–1123 (2014).
25. B. Cense, W. Gao, J. M. Brown, S. M. Jones, R. S. Jonnal, M. Mujat, B. H. Park, J. F. de Boer, and D. T. Miller, "Retinal imaging with polarization-sensitive optical coherence tomography and adaptive optics," *Opt. Express* **17**, 21634–21651 (2009).
26. K. Kurokawa, K. Sasaki, S. Makita, Y.-J. Hong, and Y. Yasuno, "Three-dimensional retinal and choroidal capillary imaging by power Doppler optical coherence angiography with adaptive optics," *Opt. Express* **20**, 22796–22812 (2012).
27. K. Kurokawa, Z. Liu, and D. T. Miller, "Adaptive optics optical coherence tomography angiography for morphometric analysis of choriocapillaris [Invited]," *Biomed. Opt. Express*, BOE **8**, 1803–1822 (2017).
28. M. J. Ju, M. Heisler, D. Wahl, Y. Jian, and M. V. Sarunic, "Multiscale sensorless adaptive optics OCT angiography system for *in vivo* human retinal imaging," *JBO, JBOPFO* **22**, 121703 (2017).
29. M. Salas, M. Augustin, L. Ginner, A. Kumar, B. Baumann, R. Leitgeb, W. Drexler, S. Prager, J. Hafner, U. Schmidt-Erfurth, and M. Pircher, "Visualization of micro-capillaries using optical coherence tomography angiography with and without adaptive optics," *Biomed. Opt. Express*, BOE **8**, 207–222 (2017).
30. A. Camino, P. Zang, A. Athwal, S. Ni, Y. Jia, Y. Jia, D. Huang, and Y. Jian, "Sensorless adaptive-optics optical coherence tomographic angiography," *Biomed. Opt. Express*, BOE **11**, 3952–3967 (2020).
31. D. X. Hammer, A. Agrawal, R. Villanueva, O. Saeedi, and Z. Liu, "Label-free adaptive optics imaging of human retinal macrophage distribution and dynamics," *PNAS* (2020).
32. R. S. Jonnal, J. Rha, Y. Zhang, B. Cense, W. Gao, and D. T. Miller, "In vivo functional imaging of human cone photoreceptors," *Optics Express* **15**, 16141 (2007).
33. F. Zhang, K. Kurokawa, A. Lassoued, J. A. Crowell, and D. T. Miller, "Cone photoreceptor classification in the living human eye from photostimulation-induced phase dynamics," *PNAS* **116**, 7951–7956 (2019).
34. M. Azimipour, D. Valente, K. V. Vienola, J. S. Werner, R. J. Zawadzki, R. J. Zawadzki, and R. S. Jonnal, "Optoretinogram: optical measurement of human cone and rod photoreceptor responses to light," *Opt. Lett.*, OL **45**, 4658–4661 (2020).

35. V. P. Pandiyan, A. Maloney-Bertelli, J. A. Kuchenbecker, K. C. Boyle, T. Ling, Z. C. Chen, B. H. Park, A. Roorda, D. Palanker, and R. Sabesan, "The optoretinogram reveals the primary steps of phototransduction in the living human eye," *Science Advances* **6**, eabc1124 (2020).
36. B. Wang, J. E. Nevins, Z. Nadler, G. Wollstein, H. Ishikawa, R. A. Bilonick, L. Kagemann, I. A. Sigal, I. Grulkowski, J. J. Liu, M. Kraus, C. D. Lu, J. Hornegger, J. G. Fujimoto, and J. S. Schuman, "In Vivo Lamina Cribrosa Micro-Architecture in Healthy and Glaucomatous Eyes as Assessed by Optical Coherence Tomography," *Investigative Ophthalmology & Visual Science* **54**, 8270–8274 (2013).
37. Z. Liu, O. Saeedi, F. Zhang, R. Villanueva, S. Asanad, A. Agrawal, and D. X. Hammer, "Quantification of Retinal Ganglion Cell Morphology in Human Glaucomatous Eyes," *Invest. Ophthalmol. Vis. Sci.* **62**, 34–34 (2021).
38. K. Kurokawa, S. Makita, Y.-J. Hong, and Y. Yasuno, "In-plane and out-of-plane tissue micro-displacement measurement by correlation coefficients of optical coherence tomography," *Optics Letters* **40**, 2153 (2015).
39. B. F. Kennedy, K. M. Kennedy, and D. D. Sampson, "A Review of Optical Coherence Elastography: Fundamentals, Techniques and Prospects," *IEEE Journal of Selected Topics in Quantum Electronics* **20**, 272–288 (2014).
40. S. Wang and K. V. Larin, "Optical coherence elastography for tissue characterization: a review," *Journal of Biophotonics* **8**, 279–302 (2015).
41. M. A. Kirby, I. Pelivanov, S. Song, L. Ambrozinski, S. J. Yoon, L. Gao, D. Li, T. T. Shen, R. K. Wang, and M. O'Donnell, "Optical coherence elastography in ophthalmology," *JBO* **22**, 121720 (2017).
42. B. Baumann, "Polarization Sensitive Optical Coherence Tomography: A Review of Technology and Applications," *Applied Sciences* **7**, 474 (2017).
43. J. F. de Boer, C. K. Hitzenberger, and Y. Yasuno, "Polarization sensitive optical coherence tomography - a review [Invited]," *Biomed. Opt. Express*, BOE **8**, 1838–1873 (2017).
44. J. F. de Boer and T. E. Milner, "Review of polarization sensitive optical coherence tomography and Stokes vector determination," *JBO* **7**, 359–371 (2002).
45. M. Pircher, C. K. Hitzenberger, and U. Schmidt-Erfurth, "Polarization sensitive optical coherence tomography in the human eye," *Progress in Retinal and Eye Research* **30**, 431–451 (2011).
46. G. Musial, S. Adhikari, H. Mirhajianmoghadam, H. M. Queener, A. W. Schill, N. B. Patel, and J. Porter, "Longitudinal In Vivo Changes in Radial Peripapillary Capillaries and Optic Nerve Head Structure in Non-Human Primates With Early Experimental Glaucoma," *Investigative Ophthalmology & Visual Science* **63**, 10 (2022).
47. S. K. Gardiner, S. Demirel, J. Reynaud, and B. Fortune, "Changes in Retinal Nerve Fiber Layer Reflectance Intensity as a Predictor of Functional Progression in Glaucoma," *Investigative Ophthalmology & Visual Science* **57**, 1221–1227 (2016).
48. X.-R. Huang, W. Kong, and J. Qiao, "Response of the Retinal Nerve Fiber Layer Reflectance and Thickness to Optic Nerve Crush," *Invest. Ophthalmol. Vis. Sci.* **59**, 2094 (2018).
49. X.-R. Huang, R. W. Knighton, Y. Z. Spector, W. Kong, and J. Qiao, "Temporal change of retinal nerve fiber layer reflectance speckle in normal and hypertensive retinas," *Experimental Eye Research* **186**, 107738 (2019).
50. B. Fortune, G. Cull, J. Reynaud, L. Wang, and C. F. Burgoyne, "Relating Retinal Ganglion Cell Function and Retinal Nerve Fiber Layer (RNFL) Retardance to Progressive Loss of RNFL Thickness and Optic Nerve Axons in Experimental Glaucoma," *Investigative Ophthalmology & Visual Science* **56**, 3936–3944 (2015).
51. X.-R. Huang, R. W. Knighton, Y. Z. Spector, and W. J. Feuer, "Cytoskeletal Alteration and Change of Retinal Nerve Fiber Layer Birefringence in Hypertensive Retina," *Current Eye Research* **42**, 936–947 (2017).
52. S. Steiner, F. Schwarzhans, S. Desissaire, H. Resch, G. Fischer, M. Pircher, C. K. Hitzenberger, and C. Vass, "Birefringent Properties of the Peripapillary Retinal Nerve Fiber Layer in Healthy and Glaucoma Subjects Analyzed by Polarization-Sensitive OCT," *Investigative Ophthalmology & Visual Science* **63**, 8 (2022).
53. M. R. Hernandez, "The optic nerve head in glaucoma: role of astrocytes in tissue remodeling," *Progress in Retinal and Eye Research* **19**, 297–321 (2000).
54. P. J. Foster, R. Buhrmann, H. A. Quigley, and G. J. Johnson, "The definition and classification of glaucoma in prevalence surveys," *British Journal of Ophthalmology* **86**, 238–242 (2002).
55. C. F. Burgoyne, "A biomechanical paradigm for axonal insult within the optic nerve head in aging and glaucoma," *Experimental Eye Research* **93**, 120–132 (2011).
56. J. Crawford Downs, M. D. Roberts, and I. A. Sigal, "Glaucomatous cupping of the lamina cribrosa: A review of the evidence for active progressive remodeling as a mechanism," *Experimental Eye Research* **93**, 133–140 (2011).
57. C. Stowell, C. F. Burgoyne, E. R. Tamm, C. R. Ethier, J. E. Dowling, C. Downs, M. H. Ellisman, S. Fisher, B. Fortune, M. Fruttiger, T. Jakobs, G. Lewis, R. H. Masland, C. H. Mitchell, J. Morrison, S. C. Sharma, I. Sigal, M. Sofroniew, L. Wang, J. Wiggs, and S. Wu, "Biomechanical aspects of axonal damage in glaucoma: A brief review," *Experimental Eye Research* **157**, 13–19 (2017).
58. E. R. Tamm, C. R. Ethier, J. E. Dowling, C. Downs, M. H. Ellisman, S. Fisher, B. Fortune, M. Fruttiger, T. Jakobs, G. Lewis, R. H. Masland, C. H. Mitchell, J. Morrison, S. C. Sharma, I. Sigal, M. Sofroniew, L.

- Wang, J. Wiggs, and S. Wu, "Biological aspects of axonal damage in glaucoma: A brief review," *Experimental Eye Research* **157**, 5–12 (2017).
59. H. Yang, J. Reynaud, H. Lockwood, G. Williams, C. Hardin, L. Reyes, C. Stowell, S. K. Gardiner, and C. F. Burgoyne, "The connective tissue phenotype of glaucomatous cupping in the monkey eye - Clinical and research implications," *Progress in Retinal and Eye Research* **59**, 1–52 (2017).
60. J. C. Downs and C. A. Girkin, "Lamina cribrosa in glaucoma," *Current Opinion in Ophthalmology* **28**, 113 (2017).
61. C. Guan, M. E. Pease, S. Quillen, Y. T. T. Ling, X. Li, E. Kimball, T. V. Johnson, T. D. Nguyen, and H. A. Quigley, "Quantitative Microstructural Analysis of Cellular and Tissue Remodeling in Human Glaucoma Optic Nerve Head," *Investigative Ophthalmology & Visual Science* **63**, 18 (2022).
62. B. Fortune, C. F. Burgoyne, G. Cull, J. Reynaud, and L. Wang, "Onset and Progression of Peripapillary Retinal Nerve Fiber Layer (RNFL) Retardance Changes Occur Earlier Than RNFL Thickness Changes in Experimental Glaucoma," *Invest. Ophthalmol. Vis. Sci.* **54**, 5653–5661 (2013).
63. L. He, H. Yang, S. K. Gardiner, G. Williams, C. Hardin, N. G. Strouthidis, B. Fortune, and C. F. Burgoyne, "Longitudinal Detection of Optic Nerve Head Changes by Spectral Domain Optical Coherence Tomography in Early Experimental Glaucoma," *Investigative Ophthalmology & Visual Science* **55**, 574–586 (2014).
64. G. Cull, C. F. Burgoyne, B. Fortune, and L. Wang, "Longitudinal Hemodynamic Changes Within the Optic Nerve Head in Experimental Glaucoma," *Investigative Ophthalmology & Visual Science* **54**, 4271–4277 (2013).
65. L. Wang, G. Cull, C. F. Burgoyne, S. Thompson, and B. Fortune, "Longitudinal Alterations in the Dynamic Autoregulation of Optic Nerve Head Blood Flow Revealed in Experimental Glaucoma," *Invest. Ophthalmol. Vis. Sci.* **55**, 3509–3516 (2014).
66. L. J. Wilsey, J. Reynaud, G. Cull, C. F. Burgoyne, and B. Fortune, "Macular Structure and Function in Nonhuman Primate Experimental Glaucoma," *Invest Ophthalmol Vis Sci* **57**, 1892–1900 (2016).
67. K. Kurokawa, J. A. Crowell, N. Do, J. J. Lee, and D. T. Miller, "Multi-reference global registration of individual A-lines in adaptive optics optical coherence tomography retinal images," *JBO* **26**, 016001 (2021).
68. J. Porter, H. Queener, J. Lin, K. Thorn, and A. A. S. Awwal, *Adaptive Optics for Vision Science: Principles, Practices, Design and Applications*, 1st ed. (Wiley-Interscience, 2006).
69. W. Drexler and J. G. Fujimoto, eds., *Optical Coherence Tomography: Technology and Applications* (Springer, 2008).
70. K. M. Hampson, R. Turcotte, D. T. Miller, K. Kurokawa, J. R. Males, N. Ji, and M. J. Booth, "Adaptive optics for high-resolution imaging," *Nat Rev Methods Primers* **1**, 1–26 (2021).
71. American National Standards Institute and Laser Institute of America, *American National Standard for Safe Use of Lasers* (Laser Institute of America, 2014).
72. F. C. Delori, R. H. Webb, and D. H. Sliney, "Maximum permissible exposures for ocular safety (ANSI 2000), with emphasis on ophthalmic devices," *J. Opt. Soc. Am. A* **24**, 1250–1265 (2007).
73. J. E. Kiske, "A scalable approach to processing adaptive optics optical coherence tomography data from multiple sensors using multiple graphics processing units," Thesis (2014).
74. B. A. Shafer, J. E. Kiske, O. P. Kocaoglu, T. L. Turner, Z. Liu, J. J. Lee, and D. T. Miller, "Adaptive-optics optical coherence tomography processing using a graphics processing unit," in *2014 36th Annual International Conference of the IEEE Engineering in Medicine and Biology Society (EMBC)* (2014), pp. 3877–3880.
75. N. H. Do, "Parallel Processing For Adaptive Optics Optical Coherence Tomography (AO-OCT) Image Registration Using GPU," Thesis (2016).
76. O. P. Kocaoglu, T. L. Turner, Z. Liu, and D. T. Miller, "Adaptive optics optical coherence tomography at 1 MHz," *Biomed. Opt. Express* **5**, 4186–4200 (2014).
77. S. A. Jabarin, "Orientation studies of poly(vinyl chloride). Part I: Intrinsic birefringence," *Polymer Engineering & Science* **31**, 638–643 (1991).
78. A. D. Slepukov, "Quantitative measurement of birefringence in transparent films across the visible spectrum," *American Journal of Physics* **90**, 625–634 (2022).
79. N. M. Jansonius, J. Nevalainen, B. Selig, L. M. Zangwill, P. A. Sample, W. M. Budde, J. B. Jonas, W. A. Lagrèze, P. J. Airaksinen, R. Vonthein, L. A. Levin, J. Paetzold, and U. Schiefer, "A mathematical description of nerve fiber bundle trajectories and their variability in the human retina," *Vision Research* **49**, 2157–2163 (2009).
80. R. L. Radius and D. R. Anderson, "The Histology of Retinal Nerve Fiber Layer Bundles and Bundle Defects," *Archives of Ophthalmology* **97**, 948–950 (1979).
81. M. Pircher, E. Götzinger, B. Baumann, and C. K. Hitzenberger, "Corneal birefringence compensation for polarization sensitive optical coherence tomography of the human retina," *JBO* **12**, 041210 (2007).
82. C. Fan and G. Yao, "Mapping local retardance in birefringent samples using polarization sensitive optical coherence tomography," *Opt. Lett.*, **OL** **37**, 1415–1417 (2012).
83. A. Dichtl, J. B. Jonas, and G. O. H. Naumann, "Retinal nerve fiber layer thickness in human eyes," *Graefe's Arch Clin Exp Ophthalmol* **237**, 474–479 (1999).

84. S. Frenkel, G. Goshen, L. Leach, J. Pe'er, M. Mimouni, and E. Z. Blumenthal, "Peripapillary distribution of Muller cells within the retinal nerve fiber layer in human eyes," *Experimental Eye Research* **166**, 91–95 (2018).
85. P. K. Yu, S. J. Cringle, and D.-Y. Yu, "Correlation between the radial peripapillary capillaries and the retinal nerve fibre layer in the normal human retina," *Experimental Eye Research* **129**, 83–92 (2014).
86. R. N. Weinreb, A. W. Dreher, A. Coleman, H. Quigley, B. Shaw, and K. Reiter, "Histopathologic Validation of Fourier-Ellipsometry Measurements of Retinal Nerve Fiber Layer Thickness," *Archives of Ophthalmology* **108**, 557–560 (1990).
87. X.-R. Huang and R. W. Knighton, "Linear birefringence of the retinal nerve fiber layer measured in vitro with a manuscript imaging micropolarimeter running head: birefringence of RNFL," *JBO* **7**, 199–204 (2002).
88. B. Cense, T. C. Chen, B. H. Park, M. C. Pierce, and J. F. de Boer, "In vivo birefringence and thickness measurements of the human retinal nerve fiber layer using polarization-sensitive optical coherence tomography," *JBO* **9**, 121–125 (2004).
89. M. Yamanari, M. Miura, S. Makita, T. Yatagai, and Y. Yasuno, "Phase retardation measurement of retinal nerve fiber layer by polarization-sensitive spectral-domain optical coherence tomography and scanning laser polarimetry," *JBO* **13**, 014013 (2008).
90. J. Dwelle, S. Liu, B. Wang, A. McElroy, D. Ho, M. K. Markey, T. Milner, and H. G. Rylander, "Thickness, Phase Retardation, Birefringence, and Reflectance of the Retinal Nerve Fiber Layer in Normal and Glaucomatous Non-Human Primates," *IOVS* (2012).
91. R. A. Jonas, Y. N. Yan, Q. Zhang, Y. X. Wang, and J. B. Jonas, "Elongation of the disc-fovea distance and retinal vessel straightening in high myopia in a 10-year follow-up of the Beijing eye study," *Sci Rep* **11**, 9006 (2021).
92. X. Chen, P. Hou, C. Jin, W. Zhu, X. Luo, F. Shi, M. Sonka, and H. Chen, "Quantitative Analysis of Retinal Layer Optical Intensities on Three-Dimensional Optical Coherence Tomography," *Invest. Ophthalmol. Vis. Sci.* **54**, 6846–6851 (2013).
93. R. W. Knighton and X.-R. Huang, "Linear birefringence of the central human cornea.," *Invest. Ophthalmol. Vis. Sci.* **43**, 82–86 (2002).
94. X.-R. Huang, R. W. Knighton, W. J. Feuer, and J. Qiao, "Retinal nerve fiber layer reflectometry must consider directional reflectance," *Biomed Opt Express* **7**, 22–33 (2015).
95. D. R. Anderson, W. F. Hoyt, and M. J. Hogan, "The fine structure of the astroglia in the human optic nerve and optic nerve head.," *Trans Am Ophthalmol Soc* **65**, 275–305 (1967).
96. J. C. Morrison, N. L. L'Hernault, J. A. Jerdan, and H. A. Quigley, "Ultrastructural Location of Extracellular Matrix Components in the Optic Nerve Head," *Archives of Ophthalmology* **107**, 123–129 (1989).
97. R. M. Goldstein and C. L. Werner, "Radar interferogram filtering for geophysical applications," *Geophysical Research Letters* **25**, 4035–4038 (1998).
98. T. Oyama, H. Abe, and T. Ushiki, "The connective tissue and glial framework in the optic nerve head of the normal human eye: light and scanning electron microscopic studies," *Archives of Histology and Cytology* **69**, 341–356 (2006).
99. S. C. Pollock and N. R. Miller, "The Retinal Nerve Fiber Layer," *International Ophthalmology Clinics* **26**, 201–221 (1986).
100. E. Wells-Gray, S. Choi, M. Slabaugh, P. Weber, and N. Doble, "Inner Retinal Changes in Primary Open-Angle Glaucoma Revealed Through Adaptive Optics-Optical Coherence Tomography," *Journal of Glaucoma* **27**, 1025–1028 (2018).
101. S. Soltanian-Zadeh, K. Kurokawa, Z. Liu, F. Zhang, O. Saeedi, D. X. Hammer, D. T. Miller, S. Farsiu, and S. Farsiu, "Weakly supervised individual ganglion cell segmentation from adaptive optics OCT images for glaucomatous damage assessment," *Optica, OPTICA* **8**, 642–651 (2021).
102. X.-R. Huang, Y. Zhou, W. Kong, and R. W. Knighton, "Reflectance Decreases before Thickness Changes in the Retinal Nerve Fiber Layer in Glaucomatous Retinas," *Invest. Ophthalmol. Vis. Sci.* **52**, 6737–6742 (2011).
103. M. Miura, S. Makita, Y. Yasuno, A. Miki, R. Nemoto, H. Shimizu, S. Azuma, T. Mino, and T. Yamaguchi, "Birefringence-derived scleral artifacts in optical coherence tomography images of eyes with pathologic myopia," *Sci Rep* **12**, 19713 (2022).
104. K. Schoenenberger, B. W. Colston, D. J. Maitland, L. B. Da Silva, and M. J. Everett, "Mapping of Birefringence and Thermal Damage in Tissue by use of Polarization-Sensitive Optical Coherence Tomography," *Appl. Opt.* **37**, 6026–6036 (1998).
105. B. Fortune, "Pulling and Tugging on the Retina: Mechanical Impact of Glaucoma Beyond the Optic Nerve Head," *Invest. Ophthalmol. Vis. Sci.* **60**, 26–35 (2019).
106. K. M. Hampson, R. Turcotte, D. T. Miller, K. Kurokawa, J. R. Males, N. Ji, and M. J. Booth, "Adaptive optics for high-resolution imaging," *Nat Rev Methods Primers* **1**, 1–26 (2021).
107. M. Azimipour, J. V. Migacz, R. J. Zawadzki, J. S. Werner, and R. S. Jonnal, "Functional retinal imaging using adaptive optics swept-source OCT at 1.6 MHz," *Optica, OPTICA* **6**, 300–303 (2019).

108. Z. Liu, F. Zhang, F. Zhang, K. Zucca, A. Agrawal, and D. X. Hammer, "Ultrahigh-speed multimodal adaptive optics system for microscopic structural and functional imaging of the human retina," *Biomed. Opt. Express*, BOE **13**, 5860–5878 (2022).
109. E. A. Boettner and J. R. Wolter, "Transmission of the Ocular Media," *Investigative Ophthalmology & Visual Science* **1**, 776–783 (1962).
110. Y. Liu, J. A. Crowell, K. Kurokawa, M. T. Bernucci, Q. Ji, A. Lassoued, H. W. Jung, and D. T. Miller, "Low-latency, photon-efficient wavefront sensing for ultrafast adaptive optics imaging of the human retina," in *Ophthalmic Technologies XXXIII* (SPIE, 2023), Vol. 12360, pp. 56–63.
111. M. Keller, Y. Liu, K. Kurokawa, B. King, and D. T. Miller, "Detecting glaucoma progression at the cellular level in the living human eye," *Investigative Ophthalmology & Visual Science* **64**, 1044 (2023).